AIAA SciTech
13-17 January 2014, National Harbor, Maryland
AIAA Atmospheric Flight Mechanics Conference

Statistical Entry, Descent, and Landing Performance Reconstruction of the Mars Science Laboratory

Soumyo Dutta,* and Robert D. Braun†
Georgia Institute of Technology, Atlanta, GA, 30332-1510, USA

The Mars Science Laboratory spacecraft landed an approximately 900 kg rover on Mars on August 5, 2012 while using the largest aeroshell and supersonic parachute ever utilized by a planetary entry mission. Similar to past Mars missions, the spacecraft recorded inertial measurement unit data and radar altimeter measurements during its descent through the Martian atmosphere, but its aeroshell was also instrumented with flush atmospheric data system sensors that captured the pressure distribution on the vehicle during hypersonic and supersonic flight regimes. The rich data set enabled a comprehensive post flight analysis of the vehicle's trajectory. This paper shows the vehicle's reconstructed trajectory, aerodynamics, and atmospheric conditions using several statistical estimation methods, specifically the Extended Kalman filter, Unscented Kalman filter, and adaptive filter. The statistical estimation methods allow for both state estimation and uncertainty quantification of model errors, which could improve design of future Mars entry missions.

Nomenclature

A	Jacobian of equations of motion with respect to state vector
B	Jacobian of equations of motion with respect to noise vector
e_0, e_1, e_2, e_3	Quaternion between inertial and planet-fixed frame
F	Force (see subscripts), N
g	Gravitational acceleration, m/s^2
H	Jacobian of measurement equation with respect to state vector
h	Measurement equation
I	Identity matrix
K	Kalman gain matrix
L	Batch size for measurement noise covariance in Adaptive filter
m	Mass, kg
n	Number of state elements
N	Batch size for process noise covariance in Adaptive filter
P	State covariance matrix
p	Pressure, Pa.
Q	Process noise covariance matrix
q_0, q_1, q_2, q_3	Quaternion between inertial and body frame
R	Measurement noise covariance matrix
r	Radius (centric), m
V	Velocity (relative), m/s
$\mathbf{v}$	Measurement noise vector
W	Weight matrix for sigma points
$\mathbf{w}$	Process noise vector
$\mathbf{x}$	State vector
$\mathbf{y}$	Measurement vector
α	Tuning term for Unscented Kalman filter

*Graduate Research Assistant, Daniel Guggenheim School of Aerospace Engineering, AIAA Student Member.
†David & Andrew Lewis Professor of Space Technology, Daniel Guggenheim School of Aerospace Engineering, AIAA Fellow.

β	Tuning term for Unscented Kalman filter
γ	Flight path angle (relative), rad
θ	Longitude, rad
κ	Tuning term for Unscented Kalman filter
λ	Tuning term for Unscented Kalman filter
ν	Bank angle, rad
ρ	Density, kg/m^3
ϕ	Latitude (centric), rad
ψ	Heading angle (relative), rad
ω	Planetary rotation rate, rad/s
$\omega_x, \omega_y, \omega_z$	Vehicle rotation rate (body frame), rad/s

Subscript

b	Backward run
f	Forward run
k	Time index
N	Normal force
T	Tangential force
u	Unscented Kalman filter

Superscript

$\bar{}$	Nominal estimate
$\hat{}$	Best estimate
$\tilde{}$	Deviation

I. Introduction

The Mars Science Laboratory (MSL) successfully landed on Mars on Aug. 5, 2012. The vehicle became the seventh, successful U.S. vehicle to complete entry, descent, and landing (EDL) on Mars and pushed the boundaries of current EDL technology.[1] The spacecraft contained on-board sensors such as 3-axis accelerometers, 3-axis gyroscopes, and radar altimeter that guided the vehicle during EDL. Moreover, MSL was also carrying an innovative aeroshell-mounted instrumentation suite, named the MSL EDL Instrumentation (MEDLI),[2] that recorded pressure measurements on the surface of the aeroshell using a flush atmospheric data system (FADS) and took in-depth temperature measurements throughout the heatshield for a large time period of the entry phase. Together, this data set provides enough independent measurements to characterize the spacecraft's trajectory, atmosphere, and aerodynamic characteristics. If statistical estimation algorithms that incorporate information about the initial state uncertainties and measurement uncertainties are applied during the reconstruction process, one can also quantify the uncertainties of the estimated parameters.

Due to the disparate measurement types present in the MSL flight data set, a comprehensive methodology is needed to utilize all of the data types to estimate as many relevant parameters, while also characterizing the parameters' uncertainties. The authors have demonstrated such a methodology in the past on simulated MSL-type data sets[3] and recent flight data from Mars Pathfinder,[4] Mars Exploration Rovers,[5] and the Phoenix lander.[6] The paper provides a background about the MSL mission and the MEDLI instrumentation. Next, the data collected on-board and used in the reconstruction is presented followed by a discussion on the reconstruction methodology itself, including the equations of motion, measurement equations, and the algorithm for the statistical estimators. Finally, the results of the trajectory and atmosphere reconstruction are presented and discussed. Extended Kalman filter (EKF), Unscented Kalman filter (UKF), and Adaptive filter are the three statistical estimation methods used for MSL reconstruction.

II. Mars Science Laboratory

MSL used a 4.5 m diameter, 70-deg. sphere-cone aeroshell that reached the limit of current launch vehicle fairing diameters.[1] The vehicle also utilized the largest Disk-gap Band (DGB) supersonic parachute ever used for a planetary mission,[7] which reached the limit of available test data for such parachutes.[8] The landed mass for MSL was around 900 kg, which was 5 times the landed mass of the previous largest rovers landed

on Mars. Additionally, the EDL system was designed to land MSL within a 25 km × 20 km ellipse, a much smaller landing footprint than any previous Mars entry spacecraft.[9] To accomplish so many unique and challenging firsts, MSL utilized a hypersonic guidance scheme and used an innovative Sky Crane landing system to drop-off the rover softly on the Martian surface. These innovative aspects of MSL's operations can be observed in the concept of operations shown in Fig. 1.[1]

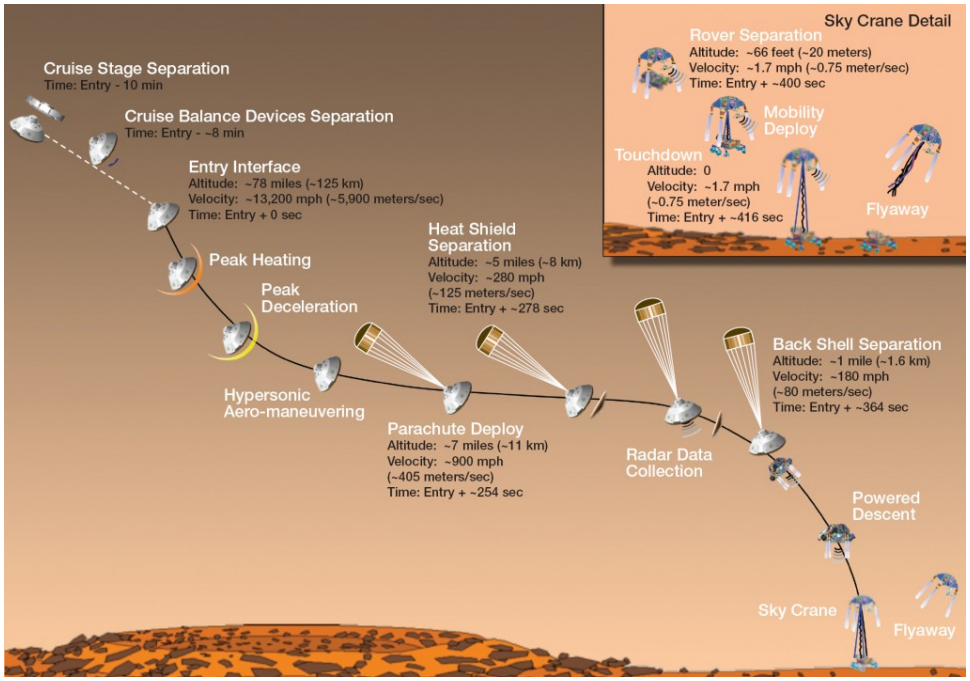

Figure 1. Mars Science Laboratory entry, descent, and landing sequence.[10]

A. Mars Science Laboratory Entry, Descent, and Landing Instrumentation

Another first for MSL was the preponderance of sensor data collected during EDL starting with the MEDLI sensors. The MEDLI suite on-board MSL took in-situ measurements of the pressure and temperature distribution on the aeroshell. It consisted of two instruments: Mars Entry Atmospheric Data System (MEADS) - a set of FADS sensors - to take the pressure measurements and MEDLI Integrated Sensor Plug (MISP) to take the aerothermodynamic data within the width of the aeroshell.[2] Since only the MEADS data aids trajectory and atmosphere reconstruction, the processing of temperature data from the MISP sensors is not covered in this paper.

MEADS's science objective is to reconstruct the atmospheric properties within certain bounds when the dynamic pressure is greater than 850 Pa. Freestream dynamic pressure (q_∞) is to be estimated within ±2% and angle of attack (α) and sideslip angle (β) are to be reconstructed within ±0.5 deg.[11] Additionally, the MEADS transducers are expected to provide surface pressure measurements to reconstruct the overall pressure distribution on the aeroshell. In order to achieve all of these targets, MEADS collects pressure data from seven pressure transducers located around the forebody of the aeroshell (see Fig. 2).

The locations of the transducers are based on the predicted pressure distribution on the aeroshell. It is expected from the nominal trajectory that the stagnation pressure is to be around transducers P1 and P2, while P4, P6, and P7 serve as the transducers that will help reconstruct the sideslip angle. All of the transducers besides P6 and P7 are expected to help reconstruct the angle of attack history.[2]

B. Collected Data

The data collected on-board MSL consists of inertial measurement unit (IMU) observations (3-axis accelerometers and 3-axis gyroscopes), radar altimeter data, and the MEADS measurements. These data were used in the reconstruction process and are presented below. Entry interface (EI) was reported at a Spacecraft Clock

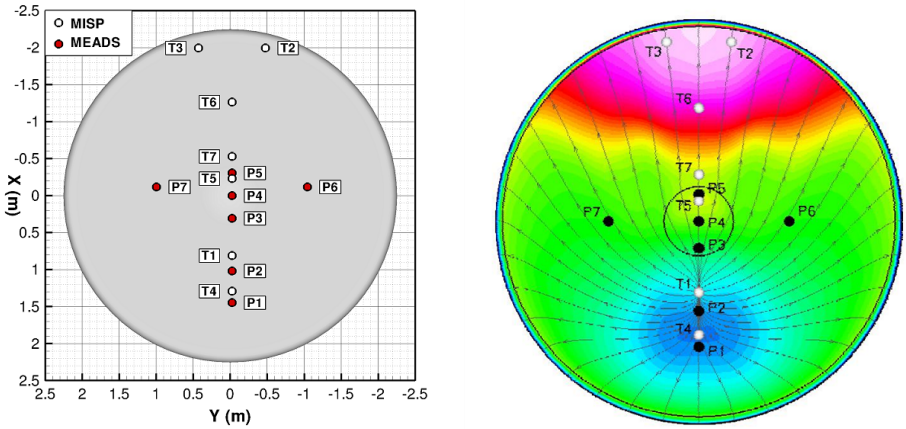

(a) Sensor locations[12] (b) Predicted flow[2]

Figure 2. MEDLI sensors.

Time (SCLK) of 397501714.953130 s and data were first collected at SCLK of 397501174.997338 s.[13,14] The data presented below have been adjusted from SCLK to an epoch where entry interface is zero.

1. *Inertial Measurement Unit Data*

The raw data collected on-board MSL consisted of δV and $\delta\theta$ measurements that were converted into accelerations and angular rates using finite differencing. The nominal sampling rate of the data were 200 Hz. Although the vehicle contained two sets of IMUs, only data from IMU-A were used during EDL by the flight controller. The reference frame for the IMU was different from typical flight dynamics convention of the body frame. The IMU frame, also referred as the Descent Stage (DS) frame, had its positive z-direction outwards in the vehicle axial direction, while the x-direction is in the pitch plane. A negative 90 deg. rotation in the y-direction brought the DS frame to the flight dynamics conventional body frame.[13] Figure 3 shows the unfiltered accelerations and angular rates in the vehicle body frame. This data were used in its unfiltered form for the reconstruction.

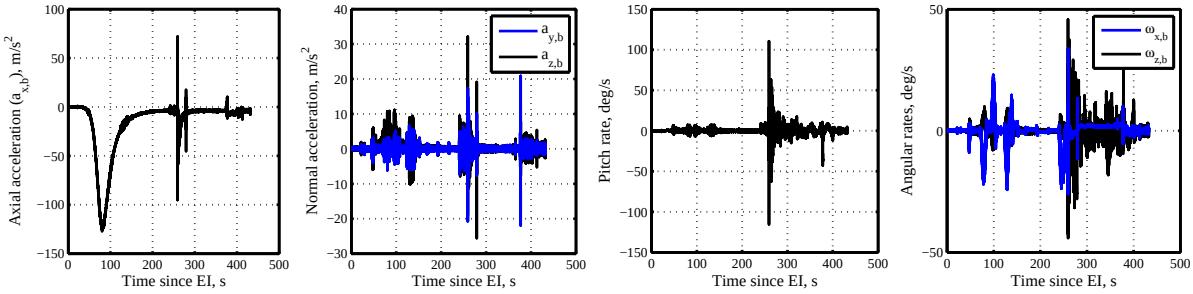

(a) Axial acceleration (b) Normal accelerations (c) Pitch rate (d) Roll and Yaw rates

Figure 3. MSL inertial measurement unit data.

2. *Terminal Descent Sensor - Radar Altimeter Data*

The radar altimeter took measurements during the terminal descent stage of the trajectory. The sensor suite consisted of several radar altimeters which collected range and range rate information. This data were processed on-board the vehicle to calculate a slant range and slant velocity. For this analysis, the slant range information was used for the trajectory reconstruction. The unfiltered 20 Hz data and the down-sampled 1 Hz data are shown in Fig. 4. Also shown is the slant range uncertainty calculated by the on-board flight software and this uncertainty was used as the measurement noise covariance in the analysis.

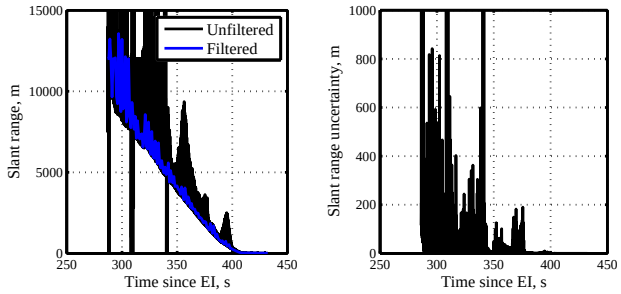

(a) Slant range (b) Slant range uncertainty

Figure 4. MSL terminal descent sensor slant range and uncertainty.

3. Mars Entry Atmospheric Data System

MEADS started collecting data from cruise stage separation at a nominal sampling rate of 8 Hz. The data were converted to engineering units using pre-flight and cruise-stage calibration data and an in-flight zero applied to the data.[14] Data were collected until shortly before the parachute mortar fire; however, the optimal calibration of the MEADS data were only guaranteed when the dynamic pressure was greater than 850 Pa. For MSL, this range fell between 50 and 175 s after EI. Only data from this restricted region is used for the analysis, although the data shown below in Figs. 5 are for all times after EI. The data were found to be close to the expected values and very little discrepancy was noticed in the initial analysis.[14]

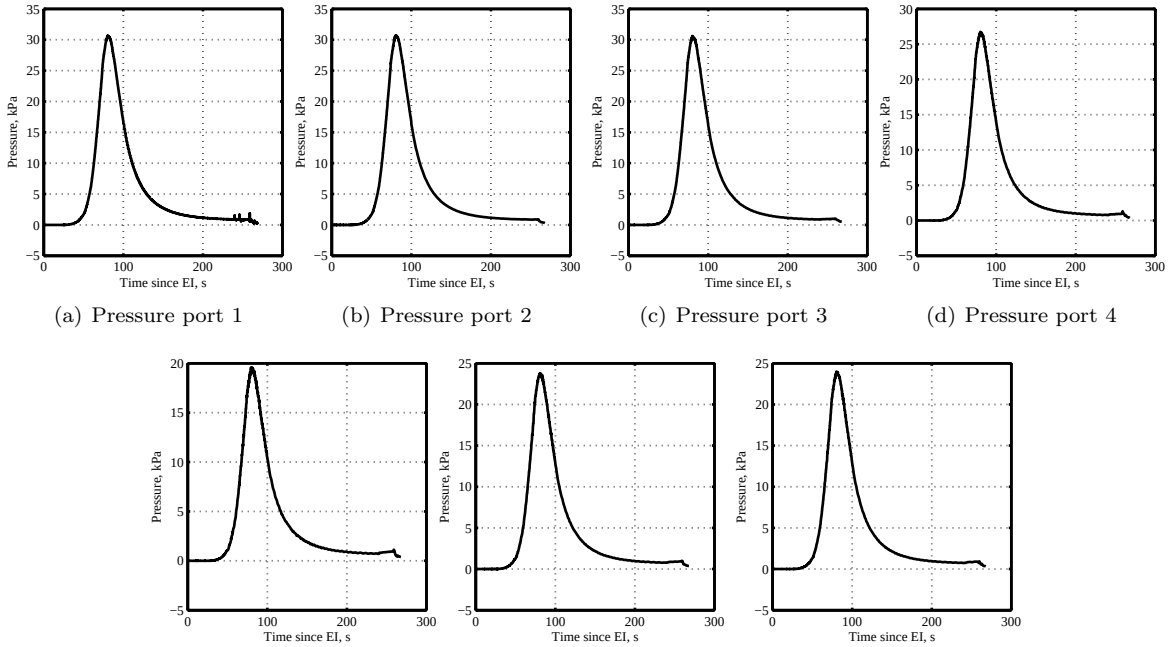

(a) Pressure port 1 (b) Pressure port 2 (c) Pressure port 3 (d) Pressure port 4

(e) Pressure port 5 (f) Pressure port 6 (g) Pressure port 7

Figure 5. MEADS data for pressure ports 1-7.

III. Reconstruction Methodology

A. Process Equations

Statistical estimation techniques similar to this methodology has been used recently for planetary entry vehicle flight reconstruction.[14,15] However, most of these analyses have used the accelerometer measurements in the process equations to propagate the velocity vector. The process equations for these methods are thus similar to the equations used by deterministic reconstructions used in the past. On the other hand,

the process equations in this paper use lift and drag coefficients estimated with the current state vector to propagate the velocity vector, thus precluding the need of accelerometer data to propagate the state vector. This also allows for the accelerometer observations to be treated as measurements by the estimation methodology. Since accelerations are a function of the sensed force on a body, which in turn depends on the freestream density and velocity, treating accelerometer data as measurements provides an additional source of measurements with which atmospheric parameters can be directly estimated in addition to FADS measurements.

The dynamical equations that serve as the process equations for all three estimators are summarized in Eqs. (1) and (10). The state vector consists of vehicle's position, velocity, attitude, freestream pressure (p_∞), and freestream density (ρ_∞) - the latter two included to capture time-varying aerodynamic states. The attitude states are given in terms of a quaternion between the inertial (J2000) and body frame (q_0, q_1, q_2, q_3) and another quaternion between the inertial (J2000) and the planet-centric, planet-fixed frame (e_0, e_1, e_2, e_3). Knowledge of the two quaternions with respect to the inertial frame provides enough information to calculate the orientation between the vehicle-carried local horizontal frame and the body frame,[16] which is needed to predict the lift and drag coefficients. The aerodynamic parameters are found using look-up tables based on the work by Dyakonov et al.[17] F_N and F_T represent the normal (lift) and tangential (drag) forces in the body axis and bank angle (ν) is used for lift modulation.

$$\dot{r} = V \sin\gamma \tag{1}$$

$$\dot{\phi} = \frac{V \cos\gamma \sin\psi}{r} \tag{2}$$

$$\dot{\theta} = \frac{V \cos\gamma \cos\psi}{r \cos\phi} \tag{3}$$

$$\dot{V} = \frac{F_T}{m} - g \sin\gamma + \omega^2 r \cos\phi \left(\sin\gamma \cos\phi - \cos\gamma \sin\phi \sin\psi\right) \tag{4}$$

$$\dot{\gamma} = \frac{1}{V}\left[\frac{F_N \cos\nu}{m} - g\cos\gamma + \frac{V^2}{r}\cos\gamma + 2\omega V \cos\phi\cos\psi + \omega^2 r \cos\phi\left(\cos\gamma\cos\phi + \sin\gamma\sin\phi\sin\psi\right)\right] \tag{5}$$

$$\dot{\psi} = \frac{1}{V}\left[\frac{F_N \sin\nu}{m\cos\gamma} - \frac{V^2}{r}\cos\gamma\cos\psi\tan\phi + 2\omega V\left(\tan\gamma\cos\phi\sin\psi - \sin\phi\right) - \frac{\omega^2 r}{\cos\gamma}\sin\phi\cos\phi\cos\psi\right] \tag{6}$$

$$\dot{p_\infty} = -\rho_\infty g V \sin\gamma \tag{7}$$

$$\dot{\rho_\infty} = -\frac{\rho_\infty^2 g V \sin\gamma}{p_\infty} \tag{8}$$

$$\begin{bmatrix} \dot{q_0} \\ \dot{q_1} \\ \dot{q_2} \\ \dot{q_3} \end{bmatrix} = \frac{1}{2}\begin{bmatrix} -q_1 & -q_2 & -q_3 \\ q_0 & -q_3 & q_2 \\ q_3 & q_0 & -q_1 \\ -q_2 & q_1 & q_0 \end{bmatrix}\begin{bmatrix} \omega_x \\ \omega_y \\ \omega_z \end{bmatrix} \tag{9}$$

$$\begin{bmatrix} \dot{e_0} \\ \dot{e_1} \\ \dot{e_2} \\ \dot{e_3} \end{bmatrix} = \frac{1}{2}\begin{bmatrix} -e_1 & -e_2 & -e_3 \\ e_0 & -e_3 & e_2 \\ e_3 & e_0 & -e_1 \\ -e_2 & e_1 & e_0 \end{bmatrix}\begin{bmatrix} 0 \\ 0 \\ \omega \end{bmatrix} \tag{10}$$

B. Extended Kalman Filter

Extended Kalman filters have been extensively used in the past for Mars EDL reconstruction and the algorithm is summarized below in Eqs. (11)- (14).[18,19]

$$\dot{P} = AP + P^T A^T + BQB^T \tag{11}$$

$$K_k = \bar{P}_k H_k^T \left(H_k \bar{P}_k H_k^T + R_k\right)^{-1} \tag{12}$$

$$\hat{\mathbf{x}}_k = \bar{\mathbf{x}}_k + K_k\left(\mathbf{y}_k - h\left(\bar{\mathbf{x}}_k\right)\right) \tag{13}$$

$$\hat{P}_k = (I - K_k H_K)\bar{P}_k(I - K_k H_k)^T + K_k R_k K_k^T \tag{14}$$

The state noise vector for EDL reconstruction comes from uncertainties in the process equations, such as aerodynamic and atmospheric uncertainties. The measurement covariance matrix (R) is defined at time k and information from sensor calibration is used in this matrix. The covariance of the state noise vector (Q) consists of noise variables in the process equations, such as the sensor uncertainty of the angular rate gyroscopes or tuning parameters for the velocity vector equations. Dutta et al.[3] discusses the values used for the state and measurement noise covariances.

C. Unscented Kalman Filter

Instead of using a linearized approximation to update the state and covariance matrix, the UKF is based on the idea that a transformation of a probability distribution can be approximated with multiple direct evaluations of an arbitrary nonlinear function.[20] UKF propagates a set of specially chosen state vectors called sigma points ($\mathbf{x}$) to characterize the transformation of the state probability distribution which are defined in Eqs. (15)-(24),[20,21] where n is the number of elements in the state space and λ_u, α_u, β_u, and κ_u are user defined tuning constants described in Refs. 20 and 22. The subscripts b and a differentiate the sigma points before and after the transformation.

$$\mathbf{x}^{(0)} = \bar{\mathbf{x}} \tag{15}$$

$$\mathbf{x}^{(i)} = \bar{\mathbf{x}} + \tilde{\mathbf{x}}^{(i)} \quad i = 1, \ldots, 2n \tag{16}$$

$$\tilde{\mathbf{x}}^{(i)} = \left((n + \lambda_u)\, P\right)_i^T \quad i = 1, \ldots, n \tag{17}$$

$$\tilde{\mathbf{x}}^{(n+i)} = -\left((n + \lambda_u)\, P\right)_i^T \quad i = 1, \ldots, n \tag{18}$$

$$W_{mean}^{(0)} = \frac{\lambda_u}{n + \lambda_u} \tag{19}$$

$$W_{covariance}^{(0)} = W_{mean}^{(0)} + 1 - \alpha_u^2 + \beta_u \tag{20}$$

$$W^{(i)} = \frac{1}{2\,(n + \lambda_u)} \quad i = 1, \ldots, n \tag{21}$$

$$\mathbf{x}^{a(i)} = h\left(\mathbf{x}^{b(i)}\right) \tag{22}$$

$$\bar{\mathbf{x}}^a = \sum_{i=0}^{2n} W^{(i)} \mathbf{x}^{a(i)} \tag{23}$$

$$P^a = \sum_{i=0}^{2n} W^{(i)} \left(\mathbf{x}^{a(i)} - \bar{\mathbf{x}}^a\right)\left(\mathbf{x}^{a(i)} - \bar{\mathbf{x}}^a\right)^T + Q_{k-1} \tag{24}$$

A new set of sigma points need to be calculated for every transformation using the process equations or the measurement equations. For the transformation using the measurement equations, one starts with the nominal estimate of the state $\bar{\mathbf{x}}$, calculates the Kalman gain in a piece-wise fashion, and then arrives at the final sigma points that define the best estimate of the state $\hat{\mathbf{x}}_k$. The predicted measurement for each sigma point ($\mathbf{y}_k^{(i)}$) and the estimate of the mean value for the predicted measurement ($\mathbf{y}_k$) can be calculated using the sigma point transformations shown in Eqs. (15)-(24). The predicted measurement covariance (P_y) and the cross covariance between the estimated state and measurement (P_{xy}) are used for the Kalman gain and state update steps shown in Eqs. (25)-(29).[20–22]

$$P_y = \sum_{i=0}^{2n} W^{(i)} \left(\hat{\mathbf{y}}_k^{(i)} - \hat{\mathbf{y}}_k\right)\left(\hat{\mathbf{y}}_k^{(i)} - \hat{\mathbf{y}}_k\right)^T + R_k \tag{25}$$

$$P_{xy} = \sum_{i=0}^{2n} W^{(i)} \left(\hat{\mathbf{x}}_k^{(i)} - \hat{\mathbf{x}}_k\right)\left(\hat{\mathbf{y}}_k^{(i)} - \hat{\mathbf{y}}_k\right)^T + R_k \tag{26}$$

$$K_k = P_{xy} P_y^{-1} \tag{27}$$

$$\hat{\mathbf{x}}_k^+ = \hat{\mathbf{x}}_k^- + K_k \left(\mathbf{y}_k - \hat{\mathbf{y}}_k\right) \tag{28}$$

$$\hat{P}_k^+ = \hat{P}_k^- - K_k P_y K_k^T \tag{29}$$

Unlike the EKF, UKF does not require the calculation of Jacobians and other derivative terms that are often computationally difficult and are sources of numerical ill conditioning. Additionally, it should be noted that other derivative-free filters, such as the divided-difference filters, are essentially variants of the UKF with minor differences in the tuning parameters for selecting the sigma points.[23]

D. Adaptive Filter

The adaptive filtering equations are used in the framework of the Extended Kalman filter. Ref. 3 lists the algorithm for this well-known filter. The innovation of the covariance-matching adaptive filter technique is that unlike the EKF, the adaptive filtering equations can compute the necessary estimation statistics when one does not have *a priori* accurate knowledge of the measurement and process noise. The approach used in this paper is summarized in Eqs. (30)- (36).[24,25]

$$\mathbf{w}_j = \hat{\mathbf{x}}_j - \bar{\mathbf{x}}_j \quad \text{j} = 1,\ldots,\text{N} \tag{30}$$

$$\hat{\mathbf{w}} = \frac{1}{N}\sum_{j=1}^{N} \mathbf{w}_j \tag{31}$$

$$\hat{Q} = \frac{1}{N-1}\sum_{j=1}^{N} B\left[\left(\mathbf{w}_j - \hat{\mathbf{w}}\right)\left(\mathbf{w}_j - \hat{\mathbf{w}}\right)^T - \left(\frac{N-1}{N}\right)\left(\bar{P}_j^* - \hat{P}_j\right)\right] B^T \tag{32}$$

$$\bar{P}_j^* = \int_{t_{j-1}}^{t_j} \left(AP + PA^T\right) dt \tag{33}$$

$$\mathbf{v}_i = \mathbf{y}_i - h\left(\bar{\mathbf{x}}_i\right) \quad i = 1,\ldots,L \tag{34}$$

$$\hat{\mathbf{v}} = \frac{1}{L}\sum_{i=1}^{L} \mathbf{v}_i \tag{35}$$

$$\hat{R} = \frac{1}{L-1}\sum_{i=1}^{L}\left(\left(\mathbf{v}_i - \hat{\mathbf{v}}\right)\left(\mathbf{v}_i - \hat{\mathbf{v}}\right)^T - \left(\frac{L-1}{L}\right) H_i \bar{P}_i H_i^T\right) \tag{36}$$

Since the exact process and measurement noise are unknown (together with the true states $\mathbf{x}$ and state covariances P), empirically derived quantities serve as surrogates to estimate the process and measurement noise. The empirically derived quantities $\mathbf{w}$ and $\mathbf{v}$ are approximations of the actual state noise and measurement noise vectors. Using these quantities, one can estimate the process noise covariance (Q) and the measurement noise covariance (R) as shown in Eqs. (32) and (36). Information from the last N state estimates are used to find $\mathbf{w}$, while information from the last L measurement points are used to calculate $\mathbf{v}$.

E. Optimal Smoothing

The reconstruction can start from atmospheric entry (forward pass) or a projected landing location (backwards pass). The forward pass starts its estimate from an initial state and covariance that is found independent of the trajectory reconstruction process and the reconstruction is conducted in a chronological manner. The backwards pass has the advantage of starting at a smaller uncertainty value as it begins from the end of the forward estimate.

Due the advantage of both types of reconstructions, the forward and backward pass estimates (denoted by the subscripts f and b respectively) are often combined using the Fraser-Potter smoothing solution[26] to create a best estimated solution. This smoothing solution is shown in Eqs. (37) and (38). It is advantageous to combine both the forward and backward estimates in finding an optimal estimate of the trajectory.[15] The forward pass estimate at time k uses the measurement data from entry to k, while the backward pass estimate at k uses the measurement data from landing time to k. The combined smoothed estimate at time k

will then use measurement data at all times to create the estimate at k and is similar to a batch least-squares solution.[27]

$$\hat{P}_k = \left[\hat{P}_{f,k}^{-1} + \hat{P}_{b,k}^{-1}\right]^{-1} \tag{37}$$

$$\hat{\mathbf{x}}_k = \hat{P}_k \left[\hat{P}_{f,k}^{-1}\hat{\mathbf{x}}_{f,k} + \hat{P}_{b,k}^{-1}\hat{\mathbf{x}}_{b,k}\right]^{-1} \tag{38}$$

IV. Results

MSL flight data are reconstructed using EKF, UKF, and Adaptive filter to provide various *best* estimates of the spacecraft's trajectory, vehicle aerodynamics, and Mars' atmosphere during EDL. In lieu of knowledge about the true states, all three reconstructions are equally plausible, so subjective comparisons between the reconstructions are made to ascertain estimation performance quality. Additionally, an independent, NASA-conducted reconstruction of the MSL data using the logic used on-board the flight software (FSW)[28] is provided where available for comparison with the three statistical estimations. The flight software reconstruction is largely a function of the IMU data.

A. Initial Conditions

The reconstruction was conducted for a time period starting at the entry interface and ending with touchdown. However, the data needed for the reconstruction were available at many different epochs. For example, IMU and MEADS data were available from cruise stage separation, while radar altimeter data became first available late into the descent phase. Moreover, the initial state estimate was available at three different epochs (EI - 9 min, 10 s; EI - 9 min; and EI) while the initial covariance was only available at EI - 9 min, 10 s. Thus, all of these values had to be brought to a standard starting epoch.

In order to find the initial conditions for all states and covariances at the entry interface, the statistical methodology was preceded by a deterministic reconstruction. The deterministic reconstruction used the IMU data to propagate the vehicle position, velocity, and attitude from EI - 9 min to touchdown. This process is similar to what was done for several past Mars EDL reconstructions.[29–31] This deterministic reconstruction was also the source of an initial estimate of freestream density and pressure. The initial freestream density prediction was found using the IMU data, assuming the perfect knowledge of aerodynamic parameters, while the initial freestream pressure was determined by integrating the hydrostatic equation with a surface pressure of 695 Pa (measured by MSL shortly after it reached the Martian surface).[14] Although this procedure confounded aerodynamic and atmospheric uncertainties, one should note that the results from these deterministic reconstructions are only used to establish the *initial conditions* for freestream density and pressure at EI; afterward, a statistical estimation method is used for reconstruction based on both IMU and FADS data for atmosphere reconstruction, eliminating the need for *perfect* knowledge of the aerodynamic parameters.

The initial conditions for MSL's state vector are summarized in Tables 1 and 2. The initial covariance at EI was found using Monte Carlo simulation with an initial state and covariance known at EI - 9 min, 10 s.

Table 1. Initial Conditions for Mars Science Laboratory (at entry interface)

State	Condition	Standard Deviation (3σ)*
Radius (centric), m	3522200	32.0662
Latitude (centric), deg	-3.9186	0.000781
Longitude (East), deg	126.72	0.000367
Velocity (inertial), m/s	6083.3	0.026059
Flight-path angle (inertial), deg	-15.4892	0.000400
Azimuth angle (inertial), deg	93.2065	0.000268
Freestream pressure, Pa†	2.973×10^{-4}	$10P_{\infty,0}$
Freestream density, kg/m^3†	2.838×10^{-8}	$10\rho_{\infty,0}$

*Found with Monte Carlo simulation with known covariance at EI - 9 min

†Determined using a deterministic reconstruction

Table 2. Initial Conditions for Quaternions (at entry interface)

	$\mathbf{q}_{J,DS}$ (J2000 to DS)	$\mathbf{q}_{J,MCMF}$ (J2000 to MCMF)
Scalar	0.0018	0.9319
i	0.4011	0.1676
j	0.4059	0.2706
k	-0.8212	0.1739

Note: Initial Euler angle uncertainties assumed to be ±0.2 deg

B. Trajectory Reconstruction

The reconstructed trajectory for MSL is shown in Fig. 6 and the estimated uncertainties for the altitude and planet-relative velocity are shown in Fig. 7. Some major EDL events can be identified on the reconstructed profile and these have been labeled in the zoomed inset of the terminal descent phase (Fig. 6(b)). Parachute deployment occurs around 260 s after EI, resulting in an inflection point in the trajectory plot, while the heatshield jettisons approximately 20 s after the parachute deployment. The next set of major events happen quickly starting with the backshell separation at 375 s, then powered approach at 378 s, and lastly Sky Crane starting at 413 s. Finally, touchdown is sensed around 430 s (7 min, 10 s) after EI.

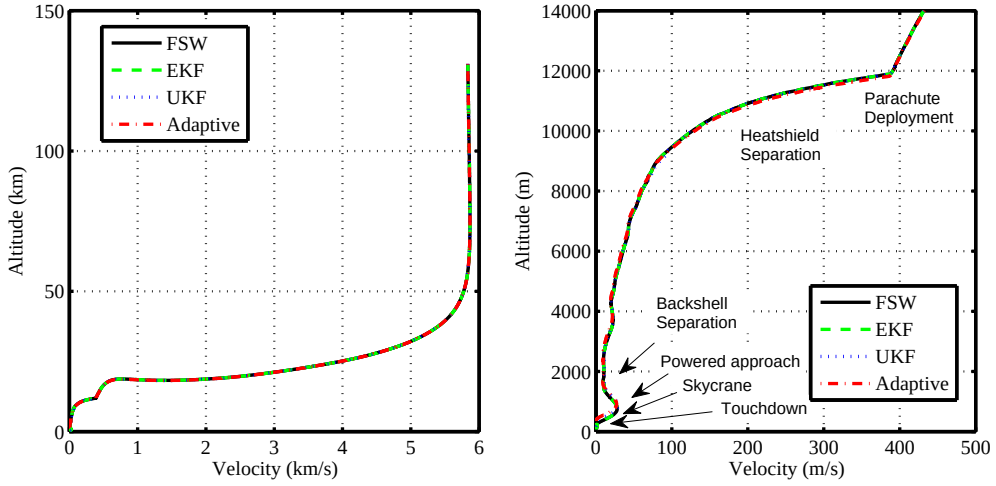

(a) Altitude vs. velocity

(b) Terminal descent (zoom)

Figure 6. Reconstructed altitude and velocity history of MSL.

There is very little difference between the reconstructed altitude and velocity profiles of the three statistical estimators and the flight software. The flight software reconstruction is largely only a function of IMU data and is conducted deterministically. The fact that the FSW reconstruction matches so closely with the statistical estimations that also used other data types is a testament to the good quality of the IMU data, which greatly improved the performance of the trajectory reconstruction. Other independent MSL data reconstructions have also noted the good quality of the IMU reconstruction.[10,14,32]

The altitude and velocity uncertainty reconstructions (Fig. 7) show that in general EKF had larger estimated uncertainties than its other statistical estimation counterparts. The EKF altitude uncertainty shows the growth in uncertainty during the hypersonic flight regime through peak deceleration around 100 s, decrease in uncertainty in the region of bank angle reversals and hypersonic guidance, a slight growth in uncertainty during parachute deployment, and finally a steady decrease in altitude uncertainty after radar altimeter data are acquired. The UKF and Adaptive filter's estimated altitude uncertainties are not as dynamic as the EKF estimate. The differences in the behavior can be directly attributed to the handling of process noise. The EKF process noise is tuned using strategies described in Ref. 3 to account for the non-linearity in the dynamics that the first-order EKF equations cannot model well. The larger process noise also leads to larger estimated state uncertainties, as was shown in the simulated data results in Ref 3. On the other hand, the UKF and Adaptive filter have higher order methods for modeling the non-linearity and process noise in the dynamics which keeps the estimate steady.

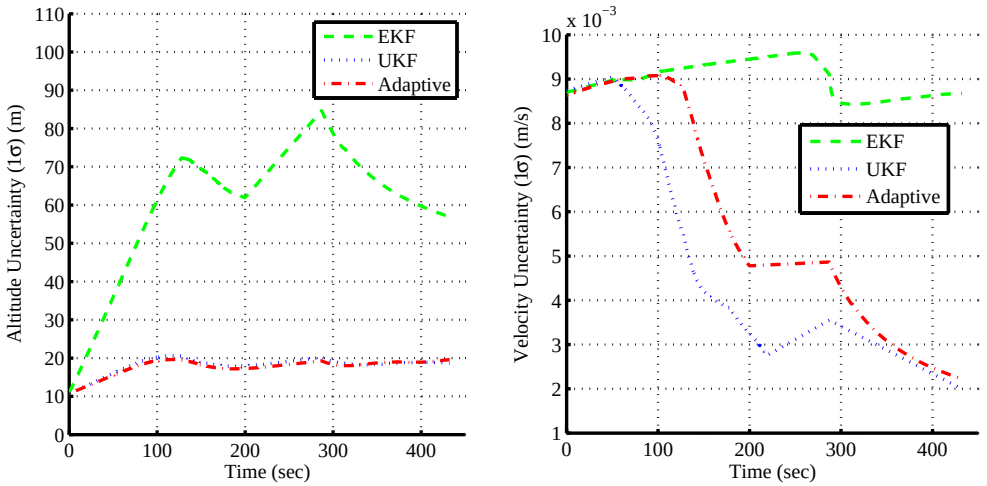

(a) Altitude uncertainty (b) Velocity uncertainty

Figure 7. Reconstructed altitude and velocity uncertainties for MSL.

The velocity uncertainties are very small, when compared to past Mars missions. This is attributed to the excellent initial velocity estimate provided by the interplanetary navigation team (as was shown in Table 1).[33] The EKF velocity uncertainty estimate does not decrease significantly from the initial estimate, but both the UKF and Adaptive estimates steadily decrease after the peak deceleration (around 100 s) and even further after radar altimeter data are acquired (near 300 s). Once again, the difference is due to the calculation of process noise. EKF has a slightly larger process noise that leads to slightly larger state uncertainty estimates. The UKF estimates smaller velocity uncertainties than the Adaptive filter in this case, but due to a lack of knowledge in the true state, it would be conjecture to attribute a physical rationale for this. Testing with simulated Mars EDL data in the past has shown that the Adaptive filter actually had smaller uncertainties than the UKF.[34]

The planet-relative flight path angle and azimuth angle histories are shown in Fig. 8. The time histories of these quantities are steady throughout the hypersonic and supersonic stages of flight, and show oscillations near the terminal descent portion when the Sky Crane was maneuvering. There is strong agreement between the reconstruction done by the three statistical estimators and the flight software estimate.

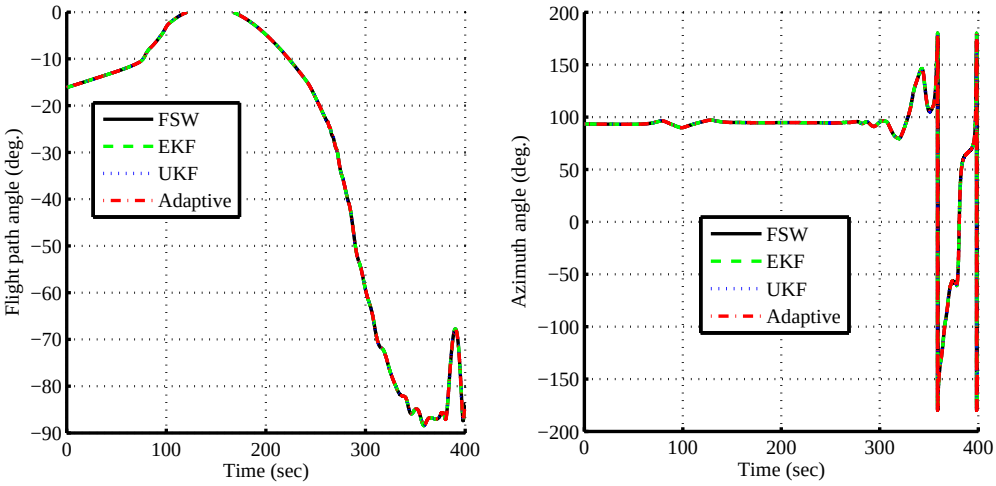

(a) Flight path angle (b) Azimuth angle

Figure 8. Reconstructed flight path and azimuth angles for MSL.

The time histories of the Euler angles - roll, pitch, and yaw - are shown in Fig. 9. Some crucial EDL events, such as bank reversals and heading alignment can be seen in these figures. The bank reversals are important since MSL was the first Mars EDL vehicle that used hypersonic guidance via bank angle

modulation.[1] These modulations are visible on the roll and yaw angle history. Heading alignment prior to parachute deployment is also observed in the figures. The Euler angle plots have been restricted to shortly before parachute deployment, since these angles have little physical meaning after that point. Similar to the case for flight path and azimuth angles, there is strong agreement between the statistically-estimated quantities and the time history reconstructed by the flight software.

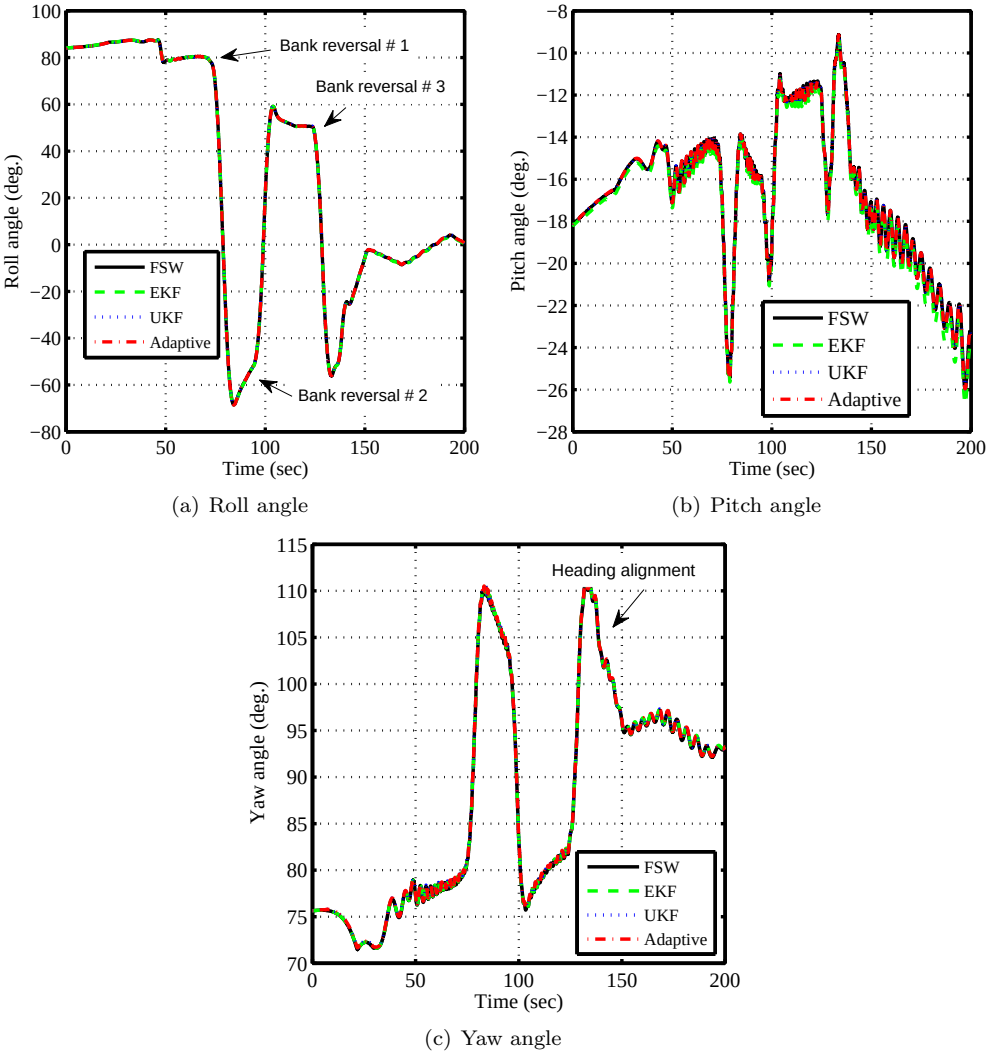

(a) Roll angle

(b) Pitch angle

(c) Yaw angle

Figure 9. Reconstructed attitude history of MSL.

Angle of attack and sideslip angle histories are shown in Fig. 10. The time axes are restricted from entry interface to the point where MEADS data were no longer processed by the estimator for Figs. 10(a) and 10(b) to showcase the region where the orientation angle estimates were influenced by both IMU and FADS data. This region is also the only place in the reconstruction where aerodynamic and atmospheric uncertainties are not confounded since two independent measurements were used to estimate the angles.

Unlike the Euler angles, there are visible differences between the estimates derived by the three statistical estimators and the flight software. The angle of attack estimates for the Adaptive filter and UKF diverge slightly from the other estimates around 100 s and then there is a step increase seen around 135 s. Similar observations were made by other independent MSL reconstructions.[32,35] The sideslip angle estimate has a difference that is more visible, since after 100 s the flight software and EKF estimates display a positive bias from zero, while the UKF and Adaptive filter estimates stay closer to zero but still display large oscillations. It is possible that the vehicle did indeed experience a non-zero sideslip angle, but a more likely explanation is a relatively significant cross wind component during this phase of flight that biases the IMU data.[10,35] Since the methodology in this paper does not estimate winds and uses the planet-relative velocity instead of the wind-relative velocity for the angle calculations, a relatively strong wind may affect the accuracy of

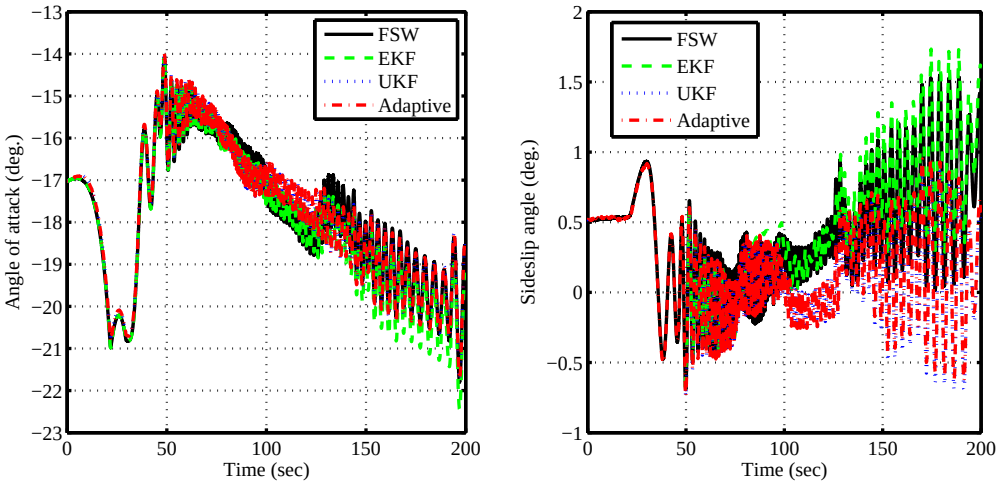

(a) Angle of attack (b) Sideslip angle

Figure 10. Reconstructed angle of attack and sideslip angle histories for MSL.

the angular estimates. The UKF and Adaptive filter are able to bias their result more towards FADS data that are theoretically not affected by the wind rather than the IMU data which are affected by the wind and thus the filters' estimate sideslip angle closer to zero.

The angle of attack and sideslip angle uncertainties are shown in Fig. 11. One can see that the introduction of MEADS data to the estimators around 50 s drastically improves the uncertainty estimates in Figs. 10(a) and 10(b). The EKF seems to have a longer lag-time before the uncertainties of the two orientation angles settle to the level of the uncertainty estimates from the UKF and Adaptive filter. In general, one sees that the 1σ uncertainties for the angle of attack are of the order 0.2 deg. and the uncertainties for the sideslip angle are close to 0.1 deg.

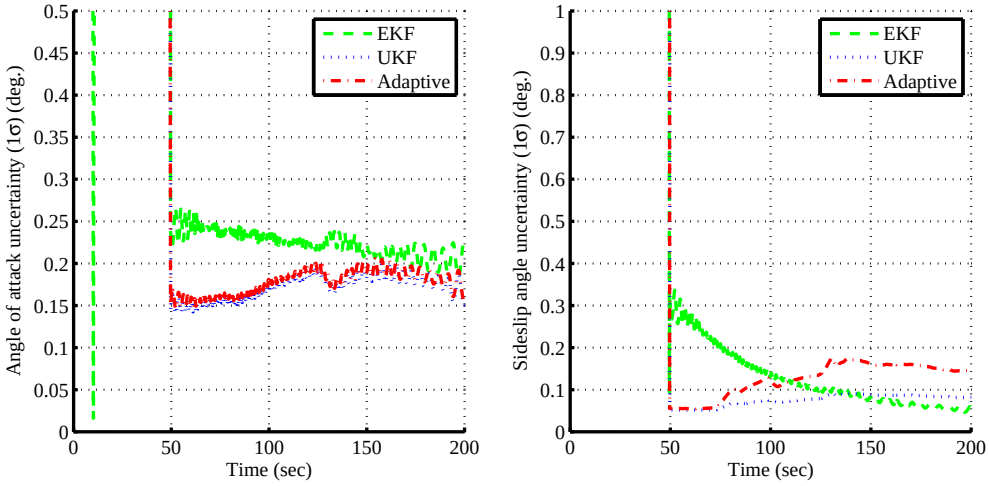

(a) Angle of attack (b) Sideslip angle

Figure 11. Reconstructed angle of attack and sideslip angle uncertainties for MSL.

The final landing location of MSL was available from post-flight communications between the rover and orbiting spacecraft.[32] This location and the reconstructed location using the estimation methodology are compared in Table 3. The 3σ uncertainty bounds of the reconstructed positions for all three estimates encompass the independently estimated location. The UKF and Adaptive filter have tighter bounds than the EKF, corroborating the expected outcomes when simulated data were analyzed by these estimators.[3,34]

Table 3. Final landing location of MSL

State	Orbit*	EKF	$3\sigma^{\dagger}$	UKF	$3\sigma^{\dagger}$	Adaptive	$3\sigma^{\dagger}$
Radius (km)	3391.13	3390.71	0.605	3391.30	0.195	3391.15	0.262
Lat. (deg)	-4.590	-4.632	0.075	-4.552	0.043	-4.557	0.045
Long. (deg)	137.442	137.394	0.0264	137.431	0.0129	137.438	0.0123

* Based on comm. between rover and orbiting satellites after landing.[32]

† Assuming a normal distribution for the parameters.

C. Atmosphere Estimation

One of the unique features of the estimation methodology is that atmospheric parameters are already included in the estimation state vector. Thus, there is no need to use the force coefficient equations or the hydrostatic equation to calculate atmospheric parameters.

Figure 12 shows the estimated atmospheric density history as well as the estimated uncertainty for the region where both IMU and FADS data were available. The value of the uncertainty generally increases with time as density increase. There is good agreement between the estimated states by the three statistical estimators, with the EKF having a slightly higher estimated uncertainty. The higher uncertainty for the EKF can be explained by the modeling of high process noise needed to avoid filter divergence. The density and uncertainties are very smooth and do not display any large oscillations. This underscores the good quality of the IMU and FADS data as well as the near-nominal atmospheric profile encountered by MSL. One does not observe any large density variations akin to the potholes-in-the-sky that were studied during the design of MSL.[36]

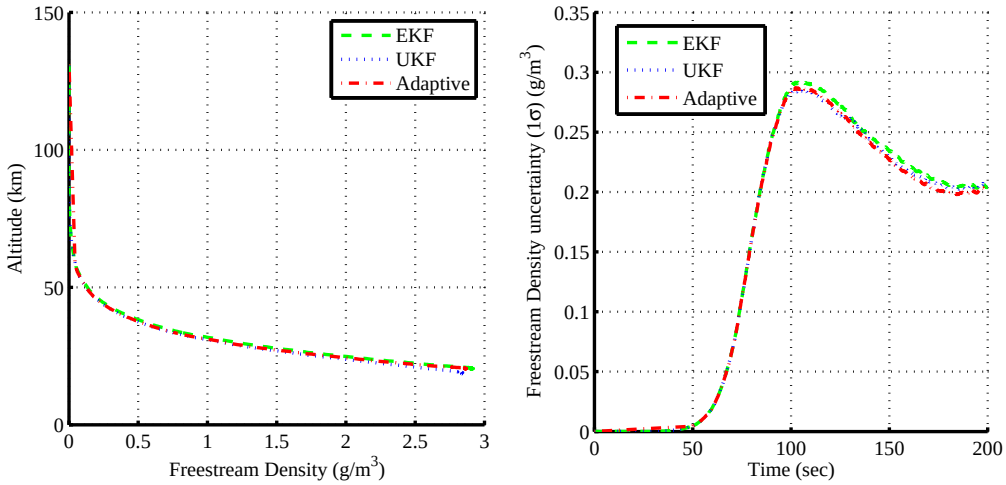

(a) Freestream density (b) 1σ uncertainty

Figure 12. Reconstructed density for MSL when FADS data was used.

Freestream pressure, which is also an element of the state vector, is shown in Fig. 13 along with the estimated 1σ uncertainty. The values are once again shown for the time period where both IMU and FADS data were available. Similar to freestream density, all three estimates show good agreement in the estimated states, while the EKF uncertainty estimate is slightly off the uncertainties estimated by UKF and Adaptive filter. The agreement between the three estimators and the smoothness of the estimates once again is a result of the good quality of the data and the near-nominal environment.

The freestream temperature, which was calculated using the reconstructed density and pressure, is shown in Fig. 14 along with the estimated uncertainty. The isothermal assumption for the hydrostatic equation and the perfect gas law were used to construct dynamical equations for freestream pressure and density. The perfect gas law was also used here to reconstruct temperature from pressure and density. However, at the top of the atmosphere before FADS data are introduced, density is estimated using accelerometer data only and since there are not enough independent measurements of density and pressure, the estimated

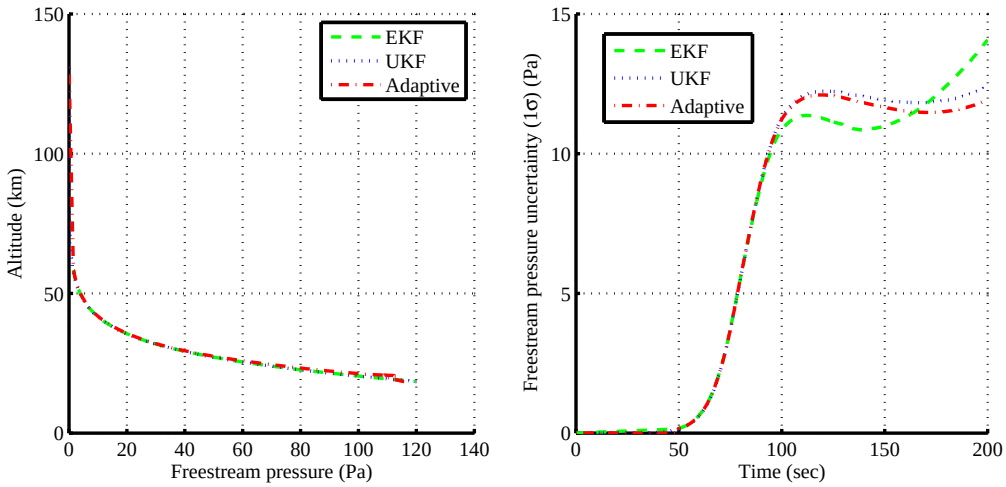

(a) Freestream pressure (b) 1σ uncertainty

Figure 13. Reconstructed pressure for MSL when FADS data was used.

temperature remains constant (isothermal). Hence, the temperature profile in Fig. 14 is limited to the points where FADS data were available. The reconstructed uncertainties for temperature show similar trends as the uncertainties for other estimated atmospheric parameters. The EKF uncertainties are slightly larger and more oscillatory than the uncertainties estimated by the UKF and Adaptive filter.

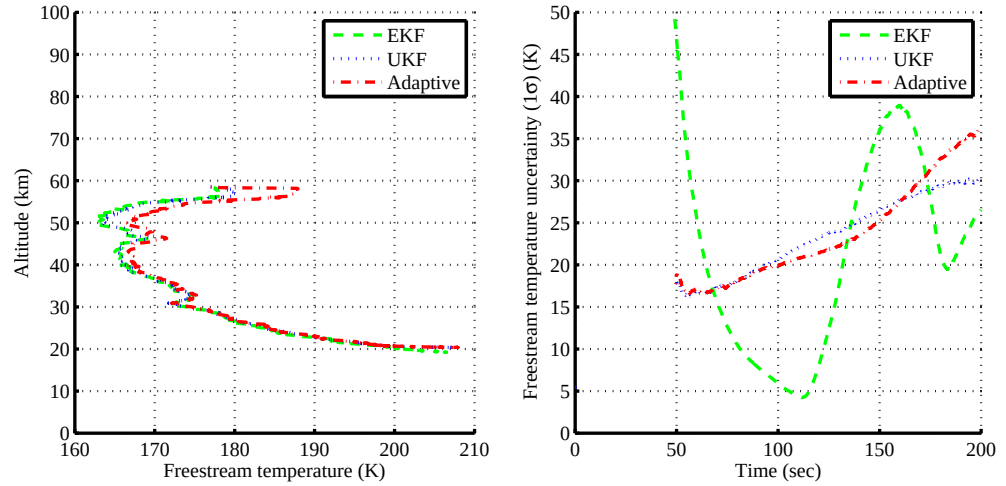

(a) Freestream temperature (b) 1σ uncertainty

Figure 14. Reconstructed temperature for MSL when FADS data was used.

The reconstructed dynamic pressure, Mach number, and their associated uncertainties are shown in Figs. 15 and 16. Dynamic pressure is calculated using the freestream pressure and planet-relative velocity, both quantities that are estimated by the methodology. Wind-relative velocity could be substituted for the planet-relative velocity for more accuracy, but the structure of this estimation methodology does not have means of estimating winds. Nevertheless, the reconstructed dynamic pressure and uncertainty agree well between the three estimators. Independent MSL reconstructions conducted by NASA also agree with these estimates.[14] Mach number was calculated using the planet-relative velocity and speed of sound calculated from freestream density and pressure. However, the uncertainties in freestream pressure and density before FADS data are introduced are also present in the speed of sound calculation, making Mach number estimates in this region highly uncertain as seen in Fig. 16(b). It is interesting to note that although the estimates of Mach number from all three estimators agree very well with each other, the uncertainty estimated by the Adaptive filter decreases rapidly after FADS data are introduced around 50 s, but there is a lag before UKF and EKF estimates reach a lower level of uncertainty. This is a sign that the Adaptive filter, which calculates

the process noise on-line, is more responsive to the lower level of uncertainty in atmospheric quantities once FADS data are introduced.

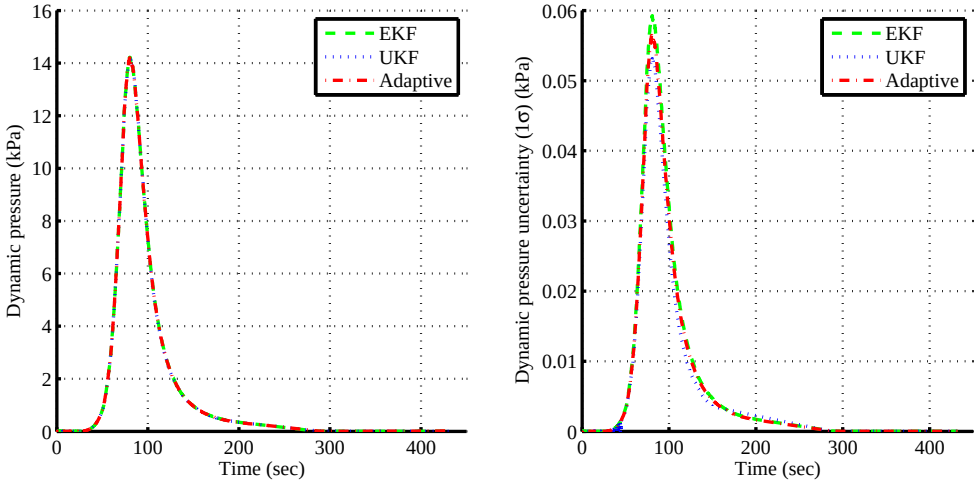

(a) Dynamic pressure (b) 1σ uncertainty

Figure 15. Reconstructed dynamic pressure and uncertainty for MSL.

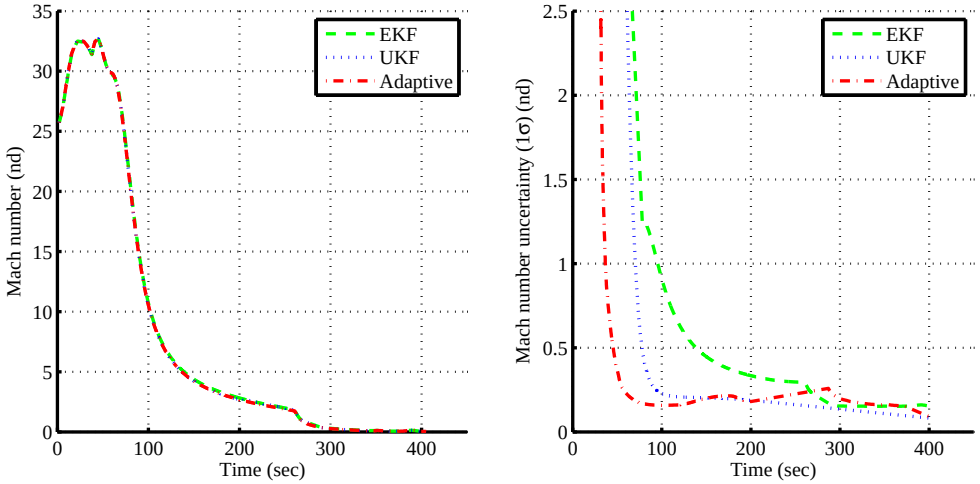

(a) Mach number (b) 1σ uncertainty

Figure 16. Reconstructed Mach number and its uncertainty for MSL.

D. Aerodynamics Reconstruction

No aerodynamic parameters were directly estimated by the three filters. Nevertheless, one can use the estimated velocity and freestream density to derive the aerodynamic quantities. Figure. 17 shows the reconstructed axial force coefficient and its 1σ uncertainty, while Fig. 18 shows the estimates for the normal force coefficient. The figures have been restricted to the region where both IMU and FADS data were available.

The unfiltered form of the accelerometer data were used in the aerodynamic coefficient estimation, hence the reconstructed force coefficients are noisy. One could have used a filtered form of the IMU data, but since the unfiltered data were used by the estimators that same data were also used for the aerodynamic reconstruction. Additionally, both axial and normal force coefficients have an increase in noise after 130 s, which is a direct result of a step increase in noise in the actual sensed axial and normal force that is visible in Fig. 19. This time does not correlate to any specific EDL event, but happens shortly before heading alignment. Of course, this is also the time where the angle of attack and sideslip angles have off-nominal behaviors (see Fig. 10), so the increase in noise is probably directly related to the effect of the winds discussed

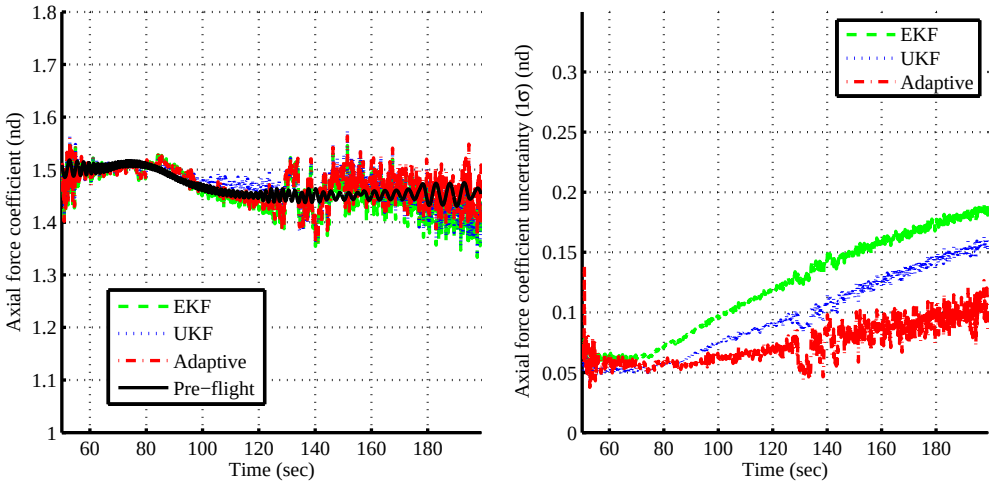

(a) Axial force coefficient (b) 1σ uncertainty

Figure 17. Reconstructed axial force coefficient and its uncertainty for MSL.

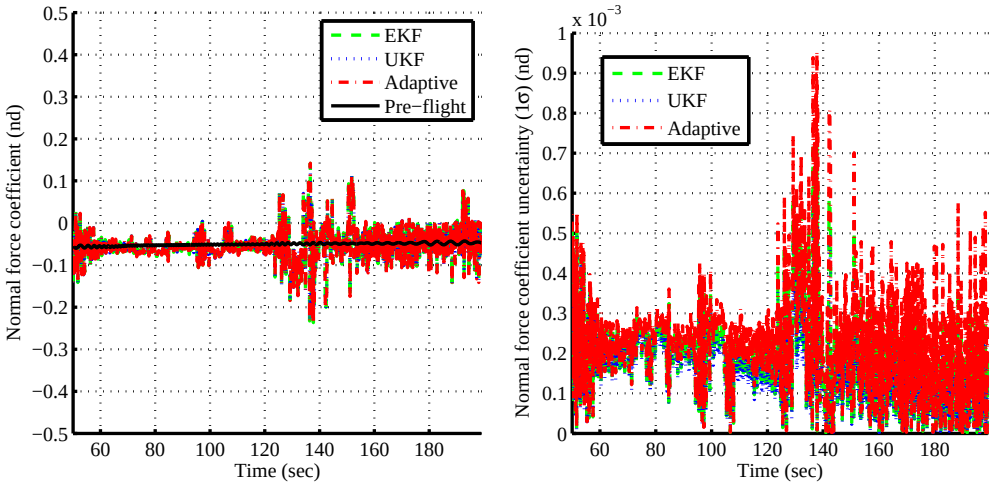

(a) Normal force coefficient (b) 1σ uncertainty

Figure 18. Reconstructed normal force coefficient and its uncertainty for MSL.

earlier.

Overall, there is good agreement between the reconstructed force coefficients found by the three filters. The UKF estimate of the axial force coefficient is slightly more oscillatory than the EKF and Adaptive estimates between 100 and 130 s, but other than that all three estimates seem to overlap. The normal force coefficient estimate is extremely noisy for all three estimates, but the reconstructed values all show a negative mean bias around -0.05. Similar observations were noted in other independent MSL reconstructions[32,35] as well, albeit with less noise since filtered-form of the IMU data were used in those cases. The axial force coefficient uncertainties show the familiar shape expected from simulated data reconstruction. The uncertainties are low when the FADS data are first introduced around 50 s, but slowly increase with time. The uncertainties also show the sign of the step increase in noise in the sensed force, since uncertainty estimates become more noisy after 130 s. There is no tell-tale shape in the normal force coefficient uncertainties, but all of the estimators have similar performance.

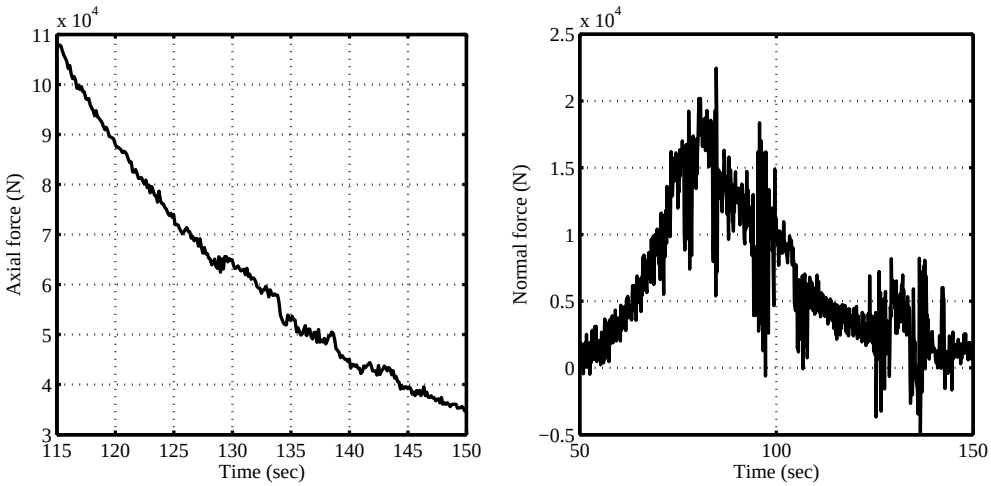

(a) Axial force (b) Normal force

Figure 19. Axial and normal forces sensed by the MSL IMU.

V. Conclusions

The Mars Science Laboratory mission demonstrated the first use of hypersonic guidance for Mars entry vehicles, and the aeroshell and supersonic parachute used by the spacecraft were the largest ever flown for Martian missions. Despite the challenges, the spacecraft safely landed on Aug. 5, 2012 in Gale Crater and relayed back inertial measurement unit data, radar altimeter measurements, and flush atmospheric data system pressure measurements that provide one of the most comprehensive data set for Mars entry vehicles.

The diversity of data from the mission makes MSL a very good test case for the statistical estimation methodology shown in this paper and developed in Ref.[3] Although parts of the process equations had to be modified to make it applicable to this case, MSL flight data were reconstructed by three different statistical estimators with great success. Overall, there was great agreement between the estimated trajectory, atmosphere, and aerodynamics found by the three estimators and the estimates compared favorably when independent reconstruction results were available. The precise initial state conditions, great quality of the flight data, and the near-nominal trajectory of MSL led to very well-behaved reconstruction results. There was generally good agreement in the estimated uncertainties found by UKF and Adaptive filter, while the EKF uncertainties were generally higher than the ones found by the other filters. Since the process noise for the EKF is not tuned on-line, the noise is usually large to keep the filter from diverging which leads to relatively larger estimates of uncertainty. The UKF and Adaptive filter are able to better accommodate the non-linearity in the dynamics and are less affected by the process noise, leading to smaller uncertainties and tighter confidence bounds.

MSL had a near-nominal trajectory, but the one unexpected behavior was the larger-than-expected winds that led to larger than nominal angle of attack oscillations and non-zero sideslip angle in the supersonic regime. The reconstruction of angle of attack and sideslip angle clearly captured this phenomenon. The FADS data were supposed to be non-susceptible to winds, while IMU data that measures sensed deceleration was susceptible to winds. The IMU-based flight software reconstruction both showed non-zero sideslip angles, while the UKF and Adaptive filter reconstructions showed sideslip angles with a mean of zero throughout the FADS data region. While the non-zero sideslip angle of the IMU-only flight software reconstruction is not unexpected, the EKF's non-zero sideslip angle is probably due to the filter's first-order state propagation equations and the way it handles process noise. While the UKF and Adaptive filter biased their estimates towards FADS data rather than IMU data in this regime and thus had near-zero sideslip angles, the EKF's process noise handling allowed the filter to be biased towards the high-rate, but wind-influenced IMU data, making the mean of the sideslip angle non-zero. This underscores the improvement in estimation capability possible as one moves from the more traditional EKF used in EDL reconstruction to higher-order filters like the UKF and Adaptive filter.

Acknowledgments

A NASA Research Announcement (NRA) award No. NNX12AF94A has supported this research. The authors want to thank Deepak Bose of NASA Ames Research Center and Chris Karlgaard, Mark Schoenenberger, and Scott Striepe of NASA Langley Research Center for their advice and help.

References

[1]Steltzner, A., Kipp, D., Chen, A., Burkhart, D., Guernsey, C., Mendeck, G., Mitcheltree, R., Powell, R., Rivellini, T., Martin, M. S., and Way, D., "Mars Science Laboratory Entry, Descent, and Landing System," IEEEAC 1497, *IEEE Aerospace Conference,* Big Sky, MT, 2006.

[2]Gazarik, M. J., Wright, M. J., Little, A., Cheatwood, F. M., Herath, J. A., Munk, M. M., Novak, F. J., and Martinez, E. R., "Overview of the MEDLI Project," IEEEAC 1510, *IEEE Aerospace Conference,* Big Sky, MT, 2008.

[3]Dutta, S., Braun, R., Russell, R., Striepe, S., and Clark, I., "Comparison of Statistical Estimation Techniques for Mars Entry, Descent, and Landing Reconstruction," *Journal of Spacecraft and Rockets*, Vol. 50, No. 6, 2013, pp. 1207–1221.

[4]Christian, J., Verges, A., and Braun, R., "Statistical Reconstruction of Mars Entry, Descent, and Landing Trajectories and Atmospheric Profiles," AIAA 2007-6192, *AIAA SPACE Conference and Exposition,* Long Beach, CA, 2007.

[5]Wells, G. and Braun, R. D., "Reconstruction of the Spirit Mars Exploration Rover Entry, Descent and Landing Performance," AA 3-2008-16, *International ARA Days Conference,* Arachon, France, 2008.

[6]Dutta, S., Clark, I., Russell, R., and Braun, R., "Statistical Entry, Descent, and Landing Performance Reconstruction of the Mars Phoenix Lander," *International Planetary Probe Workshop, Portsmouth, VA*, 2011.

[7]Schoenenberger, M., Dyakonov, A. A., Buning, P., Scallion, W., and Van Norman, J., "Aerodynamic Challenges for the Mars Science Laboratory Entry, Descent and Landing," AIAA 2009-3914, *AIAA Thermophysics Conference,* San Antonio, TX, 2009.

[8]Braun, R. D. and Manning, R. M., "Mars Exploration Entry, Descent, and Landing Challenges," *Journal of Spacecraft and Rockets*, Vol. 44, No. 2, 2007, pp. 310–323.

[9]Vasavada, A., Chen, A., Barnes, J., Burkhard, P., Canton, B., Dwyer-Cianciolo, A., Fergason, R., Hinson, D., Justh, H., Kass, D., Lewis, S., Mischna, M., Murphy, J., Rakfin, S., Tyler, D., and Withers, P., "Assessment of Environments for Mars Science Laboratory Entry, Descent, and Surface Operations," *Space Science Review*, Vol. 170, No. 1-4, 2012, pp. 793–835.

[10]Way, D. W., Davis, Jody, D., and Shidner, J. D., "Assessment of the Mars Science Laboratory Entry, Descent, and Landing Simulation," AAS 13-420*, AAS/AIAA Space Flight Mechanics Conference, Kauai, HI*, 2013.

[11]Munk, M., Little, A., Kuhl, C., Bose, D., and Santos, J., "The Mars Science Laboratory (MSL) Entry, Descent and Landing Instrumentation (MEDLI) Hardware," AAS 13-310*, AAS/AIAA Space Flight Mechanics Conference, Kauai, HI*, 2013.

[12]Edquist, K. T., Dyakonov, A. A., Wright, M. J., and Tang, C. Y., "Aerothermodynamic Design of the Mars Science Laboratory Heatshield," AIAA 2009-4075, *AIAA Thermophysics Conference,* San Antonio, TX, 2009.

[13]Essmiller, J., Brugarolas, P., and San Martin, M., "MSL EDL GN&C Reference Frames," MSL Reconstruction TIM, Sept. 2012.

[14]Karlgaard, C., Kutty, P., Schoenenberger, M., Shidner, J., and Munk, M., "Mars Entry Atmospheric Data System Trajectory Reconstruction Algorithms and Flight Results," AIAA 2013-0028*, 51st AIAA Aerospace Sciences Meeting, Grapevine, TX*, 2013.

[15]Karlgaard, C. D., Beck, R. E., Keefe, S. A., Siemers, P. M., White, B. A., Engelund, W. C., and Munk, M. M., "Mars Entry Atmospheric Data System Modeling and Algorithm Development," AIAA 2009-3916, *AIAA Thermophysics Conference,* San Antonio, TX, 2009.

[16]Kuipers, J., *Quaternions and Rotation Sequences*, Princeton University Press, Princeton, NJ, 1999.

[17]Dyakonov, A. A., Schoenenberger, M., and Van Norman, J., "Hypersonic and Supersonic Static Aerodynamics of Mars Science Laboratory Entry Vehicle," AIAA 2012-2999*, 43rd Thermophysics Conference, New Orleans, LA*, 2012.

[18]Tapley, B. D., Schutz, B., and Born, G., *Statistical Orbit Determination*, Elsevier Academic Press, Burlington, MA, 2004.

[19]Zarchan, P. and Musoff, H., *Fundamentals of Kalman Filtering, A Practical Approach*, American Institute of Aeronautics and Astronautics, Reston, VA, 2000.

[20]Julier, S., Uhlmann, J., and Durrant-Whyte, H., "A new method for the nonlinear transformation of means and covariances in filters and estimators," *IEEE Transactions on Automatic Control*, Vol. 45, No. 3, March 2000, pp. 477–482.

[21]Simon, D., *Optimal State Estimation*, Wiley-Interscience Inc., Hoboken, NJ, 2006.

[22]Lee, D.-J. and Alfriend, K. T., "Sigma Point Filtering for Sequential Orbit Estimation and Prediction," *Journal of Spacecraft and Rockets*, Vol. 44, No. 2, March 2007, pp. 388–398.

[23]Norgaard, M., Poulsen, N. K., and Ravn, O., "New developments in state estimation for nonlinear systems," *Automatica*, Vol. 36, No. 11, Nov. 2000, pp. 1627–1638.

[24]Myers, K. and Tapley, B. D., "Adaptive sequential estimation with unknown noise statistics," *IEEE Transactions on Automatic Control*, Vol. 21, No. 4, 1976, pp. 520–523.

[25]Stengel, R., *Optimal Control and Estimation*, Dover Publications, New York, NY, 1994.

[26]Fraser, D. C. and Potter, J. E., "The Optimum Linear Smoother as a Combination of Two Optimum Linear Filters," *IEEE Transactions on Automatic Control*, Vol. August, No. 31, 1969, pp. 387–390.

[27]Bell, B., "The Iterated Kalman Smoother as a Gauss-Newton Method," *SIAM Journal on Optimization*, Vol. 4, No. 3, 1994, pp. 626–636.

[28]Serricchio, F. and San Martin, M., "Mars Science Laboratory Navigation Filter," International Planetary Probe Workshop 2013, *San Jose, CA*, 2013.

[29]Desai, P. N., Prince, J. L., Queen, E. M., Schoenenberger, M., Cruz, J. R., and Grover, M. R., "Entry, Descent, and Landing Performance of the Mars Phoenix Lander," *Journal of Spacecraft and Rockets*, Vol. 48, No. 5, 2011, pp. 798–808.

[30]Spencer, D., Blanchard, R., Braun, R., Kallemeyn, P., and Thurman, S., "Mars Pathfinder Entry, Descent, and Landing Reconstruction," *Journal of Spacecraft and Rockets*, Vol. 36, No. 3, 1999, pp. 348–356.

[31]Blanchard, R. C., "Entry, Descent, and Landing Trajectory and Atmosphere Reconstruction for the Mars Exploration Rovers Missions A and B," Tech. rep., NASA-JPL Subcontract CCNS20568F, 2008.

[32]Karlgaard, C., Kutty, P., Schoenenberger, M., and Shidner, J., "Mars Science Laboratory Entry, Descent, and Landing Trajectory and Atmosphere Reconstruction," AAS 13-307*, AAS/AIAA Space Flight Mechanics Conference, Kauai, HI*, 2013.

[33]Martin-Mur, T., Kruizinga, G., and Wong, M., "Mars Science Laboratory Interplanetary Navigation Performance," AAS 13-232*, AAS/AIAA Space Flight Mechanics Conference, Kauai, HI*, 2013.

[34]Dutta, S., Braun, R., and Karlgaard, C., "Uncertainty Quantification for Mars Entry, Descent, and Landing Reconstruction Using Adaptive Filtering," *Journal of Spacecraft and Rockets*, 2013, pp. (accepted for publication).

[35]Schoenenberger, M., Van Norman, J., Dyakonov, A. A., Karlgaard, C., Way, D., and Kutty, P., "Assessment of the Reconstructed Aerodynamics of the Mars Science Laboratory Entry Vehicle," AAS 13-306*, AAS/AIAA Space Flight Mechanics Conference, Kauai, HI*, 2013.

[36]Cianciolo, A., Way, D., and Powell, R., "Effects of Atmospheric Phenomena on Mars Science Laboratory Entry Performance," AIAA 2008-6427, *AIAA/AAS Astrodynamics Specialist Conference and Exhibit,* Honolulu, HI, 2008.